AIAA JOURNAL
Vol. 48, No. 9, September 2010

Effect of Frontal Gusts on Forward Flapping Flight

Kamal Viswanath* and Danesh K. Tafti†
Virginia Polytechnic Institute and State University, Blacksburg, Virginia 24061

DOI: 10.2514/1.J050263

The response of a rigid flapping wing in forward flight, at $Re = 10,000$, subjected to frontal gusts has been investigated. The phasing and duration of the gusts and their impact on the various unsteady mechanisms are analyzed within a single flapping cycle. The gust is characterized by a step function with integral length scale much larger than that of the physical dimension of the micro air vehicle and with time scale much smaller than the flapping time period. The instantaneous lift and thrust profiles were observed to be influenced by a combination of the effective angle of attack, wing rotation, and the leading-edge vortex structures existing in the flow at any given time, with the leading-edge vortices themselves being influenced by the duration and magnitude of the change in effective angle of attack. Frontal gusts applied during the downstroke accelerated the development of the flow, resulting in the formation and detachment of multiple leading-edge vortices on the wing surface that increased the lift and thrust, illustrating the importance of the leading-edge vortex dynamics to force production. The effect of the gust is observed to be diminished when it occurs during rapid supination of the wing. The lift and thrust profiles are found to react in a similar fashion for gusts applied during the downstroke, whereas they experienced opposite effects during the upstroke. During the upstroke, force characteristics are shown to primarily react to effective angle-of-attack changes more than to changes in flow structures.

Nomenclature

$\mathbf{a}^i$	=	contravariant basis vectors
C	=	airfoil chord length
C_L	=	coefficient of lift
C_T	=	coefficient of thrust
$F_{x/y}$	=	force acting on the wing
f	=	frequency of flapping
$\sqrt{g}$	=	Jacobian of the transformation
g^{ij}	=	contravariant metric tensor
$\sqrt{g}U^j$	=	contravariant flux vector
$\sqrt{g}U_g^j$	=	contravariant flux due to grid movement
J	=	advance ratio
p	=	pressure
R	=	semiwing span, distance from flapping axis to wing tip
Re	=	Reynolds number, $U_f C/\nu$
Re_t	=	inverse of the turbulent viscosity
T	=	time period of one flapping cycle
t^*	=	nondimensional time
U_f	=	average flapping velocity of wing tip, $2\Phi f R$
U_∞	=	freestream velocity, forward-flight velocity
u_f	=	local instantaneous flapping velocity
u_i	=	Cartesian velocity vector
u_i^g	=	Cartesian grid velocity vector
$\mathbf{x}$	=	physical space coordinate
β	=	stroke plane angle
ν	=	kinematic viscosity
$\boldsymbol{\xi}$	=	computational space coordinate
ρ	=	rotation angle
Φ	=	total flapping amplitude (maximum to minimum)
ϕ	=	flapping angle
Ω_ζ	=	angular velocity of the wing
ω_ζ	=	vorticity

Subscripts

d	=	downstroke
eff	=	effective
u	=	upstroke
x, y	=	x and y directions
ζ	=	component

Received 30 September 2009; revision received 29 March 2010; accepted for publication 10 April 2010.

*Graduate Student, Department of Mechanical Engineering, 114-K Randolph Hall. Student Member AIAA.

†Professor, Department of Mechanical Engineering, 114-I Randolph Hall. Member AIAA.

I. Introduction

ONE of the requirements for a viable micro air vehicle (MAV) is the ability to withstand sudden perturbations in wind speed in the atmospheric boundary layer. Atmospheric turbulence dictated by terrain and weather conditions can potentially introduce roll, pitch and yaw disturbances. Insects and birds face a considerable challenge in sudden wind gust situations that test their capability to maneuver a desired flight path [1]. The sudden change in wing loading coupled with their inherent small inertia, like in the case of MAVs, can immediately affect flight stability. Stability in wind gust situations becomes very important, especially when they constitute a significant percent of the airspeed of the MAV.

Understanding the unsteady aerodynamics of flapping wings is critical to the design of efficient MAVs. The kinematics of wing motion is often a complex combination of translation and rotation in the stroke plane with significant morphological changes for optimal flow control. A number of aerodynamic mechanisms such as *clap and fling* [2], *delayed stall* [3], *wake capturing* [4], and *rotational circulation* [4] have been proposed to explain the generation of lift in birds and insects. Although delayed stall explains the lift generated during the translational kinematics, *rotational circulation* and *wake capture* mechanisms are proposed for the high lift produced during the rotational period. However, the validity of these models is unclear and some studies [5,6] have provided alternate reasoning for enhanced force production during the rotational period. However, since wing translation usually comprises a major part of the kinematics, the leading-edge vortex (LEV) dynamics (delayed stall) are some of the most influential factors affecting overall lift generated by a flapping wing [3].

Many of the numerical studies involving flapping flight have focused on hovering models [7–11]. Previous analysis of forward flight done by Gopalakrishnan and Tafti [12] at $Re = 10,000$ and at advance ratio $J = 0.5$ showed the presence of a strong spanwise flow along the core of the LEV similar to that of flow visualization studies conducted by Ellington [13]. In addition they found that the LEV became unstable near the wing tip before midstroke. The LEV

instability was attributed to the tip vortex blocking the removal of vorticity by impeding the spanwise flow, leading to vorticity buildup and subsequent instability. The effect of different Reynolds numbers and tip shapes on force production for flapping flight was also investigated by Gopalakrishnan and Tafti [14], who found the presence of strong spanwise flow even at $Re = 100$, which was in contrast to previous studies [15]. They also found that the different tip shapes considered in their study did not substantially affect LEV formation and breakup nor was there any substantial effect on lift and thrust production during the flapping cycle. Gopalakrishnan and Tafti [16] investigated the effect of flexible wings, approximated as linear elastic membranes with different prestresses. They found that the aerodynamic force induced camber played a major role in improving performance by keeping the LEV close to the wing top surface.

Gusts are most commonly simulated [17,18] as sudden velocity increases from the desired direction of attack onto the wing. When considering frontal gusts and forward flight, increasing the mean velocity of the airflow incident on the wing is akin to increasing the advance ratio of the simulation. Ramamurti and Sandberg [17] recently investigated the effect of downward gust on the hovering *Drosophila melanogaster*. They found that the rotational forces responsible for peaks in thrust and drag just before stroke reversal diminished with increasing downward gust velocity, and the wake capture mechanism that facilitates thrust production vanishes when the gust velocity equals the mean wing-tip velocity. Lian and Shyy [18] examined the effect of a head on gust on a plunging and pitching airfoil with a flapping frequency approximately seven times the gust frequency and found that there was a phase lag between the gust variation and the response from the airfoil. However, neither the effect of the gust on lift and thrust production mechanisms was explored nor the effect of a gust with a frequency higher than the flapping frequency was considered. Gopalan and Povitsky [19] investigated gust suppression by flapping airfoils, with the goal of enhancing lift to negotiate the sudden change in flight conditions for MAVs. Two-dimensional rigid airfoils are taken as prototypes of MAVs and a sinusoidal gust is applied to pure pitch and pure plunge motions of the airfoil to test their sensitivity. They concluded that the pure pitch motion smoothes out the freestream disturbance better, whereas the pure plunge motion is able to suppress the oscillations in the lift forces more effectively. A zero phase lag between the applied gust and lift/thrust forces was reported.

The flying speed of a MAV is approximately 10–20 m/s and it is expected that it will mostly fly within 100 m from the ground, where the atmospheric boundary layer and wakes shed by ground objects are also anticipated to play a significant role. Freestream disturbances on flapping flight can be characterized by considering the integral length λ and time scale τ of the disturbance with respect to the characteristic length and time scales of the MAV given by the chord or flapping amplitude Λ and the flapping period T, respectively. For example, $\lambda \ll \Lambda$ and $\tau \ll T$ asymptotes to disturbances having the characteristics of freestream turbulence. At these small scales, the exact temporal and spatial form of the disturbances may not be that important: only that the disturbances behave like small-scale turbulence and impact the flow development around the flapping wing throughout the cycle. At the other extreme, a disturbance with $\lambda \gg \Lambda$ and $\tau \gg T$ asymptotes to a quasi-steady behavior. For example, a sustained $\tau \gg T$ change in freestream velocity that engulfs ($\lambda \gg \Lambda$) a forward-moving MAV can be effectively analyzed by considering the two advance ratios independently, before and after the disturbance, once the transient between the two states has passed. In fact, the disturbances analyzed by Ramamurti and Sandberg [17] and Lian and Shyy [18] fall in this category. Similarly, two other asymptotic disturbances can be defined: one during which the flapping wing is subjected to multiple spatially uniform disturbances during a flapping cycle ($\lambda \gg \Lambda$ and $\tau \ll T$) and the other in which the wing is subjected to a temporally invariant but spatially varying disturbance ($\lambda \ll \Lambda$ and $\tau \gg T$). Although natural disturbances are infinitely diverse in form and structure, the investigation of near-asymptotic states allows a systematic evaluation of the dynamics and lends itself to a better characterization of cause and effect.

It is the objective of this paper to investigate disturbances of type $\lambda \gg \Lambda$ and $\tau < T$ by perturbing the freestream velocity using a square waveform. This is accomplished by changing the advance ratio J from 0.5 to 1.0 and vice versa, simulating a sudden wind gust for a prescribed time interval during the cycle. Our intent is to examine the effect of the gust on flow structure in the vicinity of the wing and the resulting instantaneous effect on lift and thrust profiles. The effect of varying the timing and duration of the gust and its phasing with respect to the flapping cycle is analyzed. The kinematic parameters are also varied in order to analyze their effect in combination with the freestream disturbances. Table 1 shows some of the possible ranges of the dimensional parameters for the chosen nondimensional values in this simulation. As can be seen, a wide range of relevant flapping frequencies and flapping amplitudes are possible within the given framework.

II. Methodology

In the present study, a structured multiblock solver with a boundary-fitted dynamic grid is employed. In this framework the grid deforms with the wing motion. The method of large-eddy simulations is employed with a subgrid stress model to resolve the turbulence in the flowfield. The governing equations for unsteady incompressible viscous flow in a moving coordinate system consist of space, mass, and momentum conservation laws. The equations are mapped from physical $\mathbf{x}$ to logical/computational space $\boldsymbol{\xi}$ by a boundary conforming transformation $\mathbf{x} = \mathbf{x}(\boldsymbol{\xi})$, where $\mathbf{x} = (x, y, z)$ and $\boldsymbol{\xi} = (\xi, \eta, \zeta)$. The equations are nondimensionalized by chord length C, flapping velocity U_f, and a derived characteristic time scale of C/U_f and written in conservative nondimensional form as

Space:

$$\frac{\partial}{\partial t}(\sqrt{g}) - \frac{\partial}{\partial \xi_j}(\sqrt{g}U_g^j) = 0 \tag{1}$$

Mass:

$$\frac{\partial}{\partial \xi_j}(\sqrt{g}U^j) = 0 \tag{2}$$

Momentum:

$$\frac{\partial}{\partial t}(\sqrt{g}u_i) + \frac{\partial}{\partial \xi_j}([\sqrt{g}U^j - \sqrt{g}U_g^j]u_i) = -\frac{\partial}{\partial \xi_j}(\sqrt{g}(\mathbf{a}^j)_i p) + \frac{\partial}{\partial \xi_j}\left(\left(\frac{1}{Re} + \frac{1}{Re_t}\right)\sqrt{g}g^{jk}\frac{\partial u_i}{\partial \xi_k}\right) \tag{3}$$

where $\mathbf{a}^i$ are the contravariant basis vectors, $\sqrt{g}$ is the Jacobian of the transformation, g^{ij} is the contravariant metric tensor, $\sqrt{g}U^j = \sqrt{g}(\mathbf{a}^j)_k u_k$ is the contravariant flux vector, $\sqrt{g}U_g^j = \sqrt{g}(\mathbf{a}^j)_k u_k^g$ is the contravariant flux vector, due to grid velocity u^g, u_i is the

Table 1 Range of dimensional parameters for the chosen nondimensional variables

Wing span, m	Chord length, m	Flapping amplitude Φ, deg	Average flapping velocity U_f, m/s	Freestream velocity U_∞, m/s	Frequency f, Hz
0.08	0.02	60°	8	4	48
0.08	0.02	120°	8	4	24
0.1	0.025	120°	6.4	3.2	15
0.16	0.04	60°	4	2	12

Cartesian velocity vector, and p is the pressure. In the above formulation, the grid velocity u^g is not used explicitly. Instead, the grid contravariant flux vector is employed, which is directly computed based on the space conservation law (SCL). The Reynolds number is given by $U_f C/\nu$. Re_t is the inverse of the subgrid eddy viscosity, which is modeled as

$$\frac{1}{Re_t} = C_s^2(\sqrt{g})^{2/3}|\bar{S}| \tag{4}$$

where $|\bar{S}|$ is the magnitude of the strain rate tensor given by $|\bar{S}| = \sqrt{2\bar{S}_{ik}\bar{S}_{ik}}$ and the Smagorinsky constant C_s^2 is obtained via the dynamic subgrid stress model (Germano et al. [20]).

The equations are formulated in a finite volume framework using a fractional-step algorithm for time advancement. Second-order central differences are used for the convective and viscous terms and a combination of an explicit Adams–Bashforth and implicit Crank–Nicolson discretizations are used for time advancement. During the start of each time step, the wing is moved based on the prescribed kinematics, keeping the external boundaries of the computational domain fixed. The resulting grid movement is carried out at each time step by a combination of a spring analogy and transfinite interpolation on displacements [21,22]. The SCL [Eq. (1)] is used to calculate the grid contravariant fluxes [21,22] that are used in the momentum equations to account for grid movement.

III. Numerical Setup

The study is done for flapping flight at Reynolds number 10,000 with characteristic length and velocity scales as chord length C and flapping velocity U_f, respectively. An infinitesimally thin rectangular rigid wing with aspect ratio of 4, as shown in Fig. 1 is used for the analysis. A single wing configuration with a symmetry boundary condition along the flapping axis is employed in the current study assuming that there is no interference between wings, and between fuselage and wing. The rotation axis is placed at the quarter-chord length from the leading edge. The downstream boundary is placed at 15 chord lengths from the trailing edge, and 10 chord lengths are used for other boundaries. Constant-velocity boundary condition is applied at all inlet faces and an outflow boundary condition is specified downstream. A symmetry condition is applied at the base of the wing. The grid consists of 60 blocks with approximately 6.5 million cells. The wing is resolved using 80×40 grid points, and 80 grid points are used perpendicular to the wing, as shown in Fig. 2. At this resolution, one flapping period on 60 processors of System-X at Virginia Polytechnic Institute and State University consumed a wall-clock time of approximately 20 h.

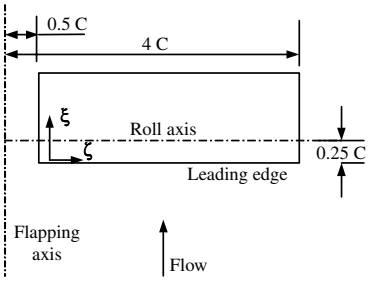

Fig. 1 Rectangular wing configuration.

A grid refinement study for the current grid has been carried out by Gopalakrishnan and Tafti [12] by increasing the number of grid points along the perpendicular direction from 80 to 120. The comparison of instantaneous lift and thrust forces showed no perceptible change and the mean values of lift and thrust differed by less than 1%. Validation cases related to the dynamic mesh capability of the solver in predicting the wake structure and force response of an oscillating cylinder in crossflow, and the change from a drag-producing to a thrust-producing wake in a heaving airfoil are available in previous studies [23]. In the case of a heaving airfoil, the analysis was carried out at different plunging velocities to obtain different wake structures, which showed excellent agreement with the flow visualization experiments of Lai and Platzer [24] and the quantitative measurements of lift coefficients and propulsive efficiency by Heathcote et al. [25]. Further, an analysis of hovering fruit fly was also carried out by Gopalakrishnan and Tafti [26] and reasonable agreement with the experimental results of Sane and Dickinson [27] were obtained.

The effect of the distance of the domain boundaries from the wing surface on the flow features resolved was also investigated. Domain boundaries too close to the wing could potentially adversely influence flow features by forcing freestream conditions at the upper, lower, and flanking boundaries thus not allowing unsteady transient flow structures to manifest correctly. Boundaries too far away from the wing surface could potentially lead to unnecessary computations or an unnecessarily course grid. To this effect, another refinement study is done by shrinking the domain length in all directions around the wing while keeping the number of grid points the same and only changing their distribution. The resulting grid distribution is compared to the original distribution in Figs. 3–5. The downstream boundary is shortened to eight chord lengths (down from 15) (Fig. 3) and the upstream boundary to six chord lengths (down from 10), and the lower and upper boundaries only extend until six chord lengths (down from 10) (Fig. 4). The domain length in the spanwise direction is nine chord lengths (down from 14) (Fig. 5). Keeping the number of grid points the same facilitates much denser grid spacing and more grid points in the close vicinity of the wing surface. A comparison of the results obtained from the two domain sizes shows good agreement on instantaneous lift and thrust forces, with the mean values differing by less than 1%.

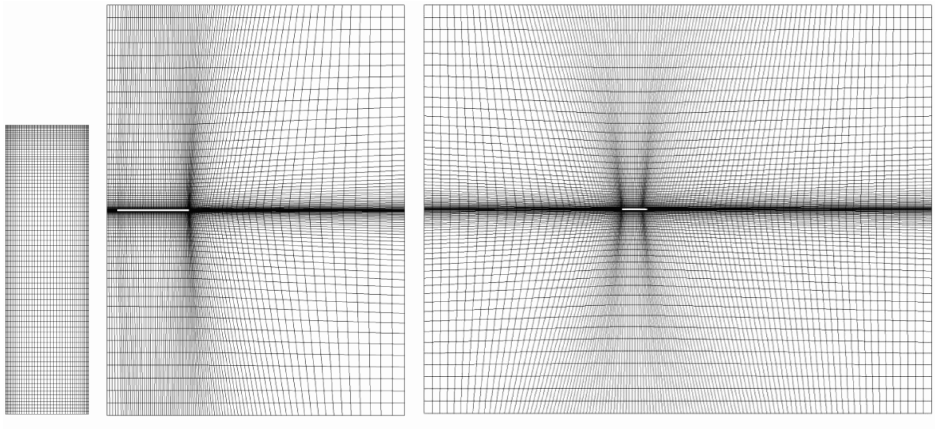

Fig. 2 Grid distribution: a) wing, b) spanwise plane, and c) chordwise plane (every other grid line is shown for spanwise and chordwise).

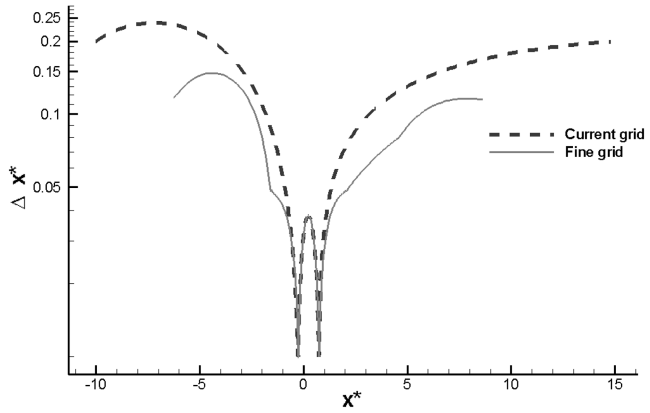

Fig. 3 Variation of spacing in the x^* direction.

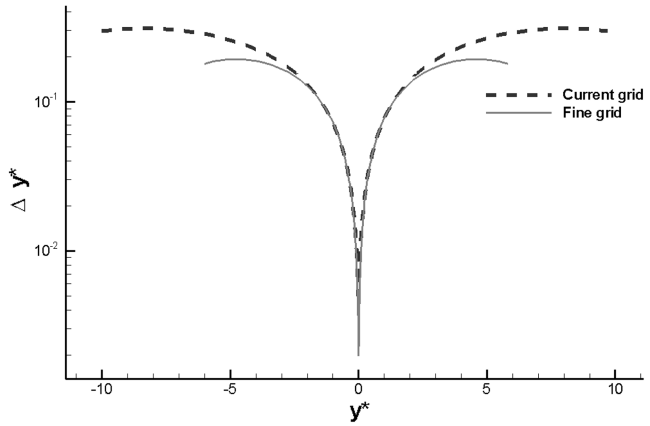

Fig. 4 Variation of spacing in the y^* direction.

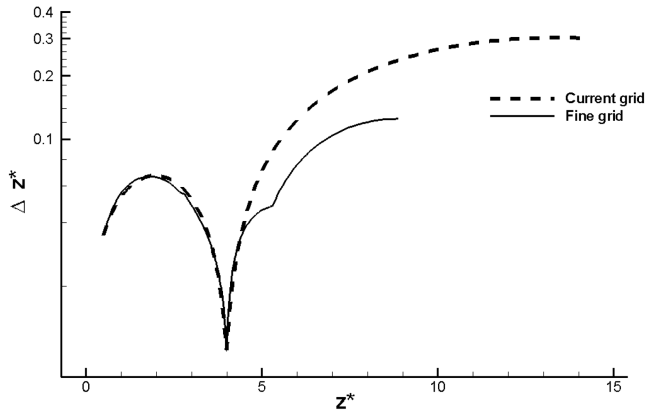

Fig. 5 Variation of spacing in the z^* direction.

Table 2 gives the definition of some of the oft used terms in flapping flight literature and Fig. 6 shows their 3-D depictions. The flapping cycle typically consists of a translational downstroke followed by wing rotation (supination), an upstroke, and again wing rotation (pronation) to complete the cycle. The term continuous rotation is used when the wing rotation is superimposed on the translational phases of the cycle. The flapping kinematics used in this study involve a cosine wave form with a stroke plane angle of $\beta = 90°$. Figure 7a shows a two-dimensional representation of the wing midchord motion for one cycle with continuous rotation, and Fig. 7b shows the variation of the flapping angle and the rotation angle ρ or angle of attack ($\alpha = 90 - \rho$) at midspan during a flapping cycle for different rotational kinematics. The flapping angle follows a cosine variation starting at $+30°$ at the beginning of the downstroke to $-30°$ at the end of the downstroke at $t^* = 0.5$. Different rotation kinematics, namely advanced rotation with duration $t^* = 0.1$, and continuous rotation are used to study the effect of gusts. The different rotational kinematics are characterized by plotting the rotation angle ρ in Fig. 7; in continuous rotation, ρ changes continuously during the cycle, whereas in advanced rotation, the change in ρ occurs at the end of the translational phases but is advanced compared to symmetric rotation. In all cases, a large ρ is used during the upstroke to reduce the angle of attack ($\alpha = 90 - \rho$) to reduce the downward force on the wing.

IV. Results

For fixed wings, the angle of attack is constant across the span of the whole wing. For flapping wings, hinged at the root, the air deflection is different, due to a changing *effective* angle of attack (AOA) α_{eff} from root to wing tip. In addition to the wing rotation angle ρ, the effective angle of attack α_{eff} is affected by both the local flapping velocity and freestream velocity as given in Fig. 8. Figures 9a and 9b show the variation of α_{eff} during the flapping cycle for continuous and advanced rotational kinematics, respectively, at the midspan of the wing for two advance ratios, $J = 0.5$ and 1.0, which characterize the wind gust. For continuous rotation, α_{eff} increases during the downstroke, reaches a plateau at $t^* = 0.15$ and then drops gradually as the motion transitions into the upstroke. In advanced rotation, α_{eff} increases until $t^* = 0.25$, plateaus but then increases again during the advanced rotation phase before moving into the upstroke. It is noted that the application of the wind gust is characterized by a sudden drop in α_{eff} during the downstroke followed by a sudden increase on removal. Conversely, the opposite sequence occurs in an inverse gust (decreasing velocity). Although Fig. 9 only shows the time variation at wing midspan, α_{eff} also varies along the span from base to tip with a maximum value at the tip, due to the variation of local flapping velocity u_f. This spanwise variation in α_{eff} introduces three-dimensionality into the flow structures in a hinged flapping wing as opposed to the intrinsic two-dimensional structures in plunging airfoils. For example, for an advance ratio of $J = 0.5$ during the downstroke, α_{eff} varies from $-20°$ to $55°$ from base to tip, whereas during the upstroke, the value of α_{eff} varies from 45 to $-30°$. The formation and structure of the spiral LEV at the leading edge during the downstroke follows the trend in α_{eff} of increasing in size from base to tip until it interacts with the tip vortex.

Table 2 Kinematic parameters and nondimensional numbers for flapping flight

Parameters	Description
Stroke plane	The plane defined by three points: wing base B and the wing tip at maximum T_T and minimum angular position T_B shown in Fig. 6. During hovering the stroke plane will be near horizontal, and during forward flight it will be vertical.
Stroke plane angle β	Angle between the stroke plane and the horizontal plane. It ranges from 0° for hovering to 90° for forward flight.
Angle of attack α	Angle between the wing chord (from trailing edge to leading edge) and the direction of motion.
Wing rotation angle ρ	Angle between the wing chord and the direction perpendicular to stroke plane.
Flapping angle ϕ	Angle between the leading edge of the wing and the plane perpendicular to the stroke plane.
Supination	Rotation of the wing at the end of downstroke preceding upstroke
Pronation	Rotation of the wing at the end of upstroke preceding downstroke

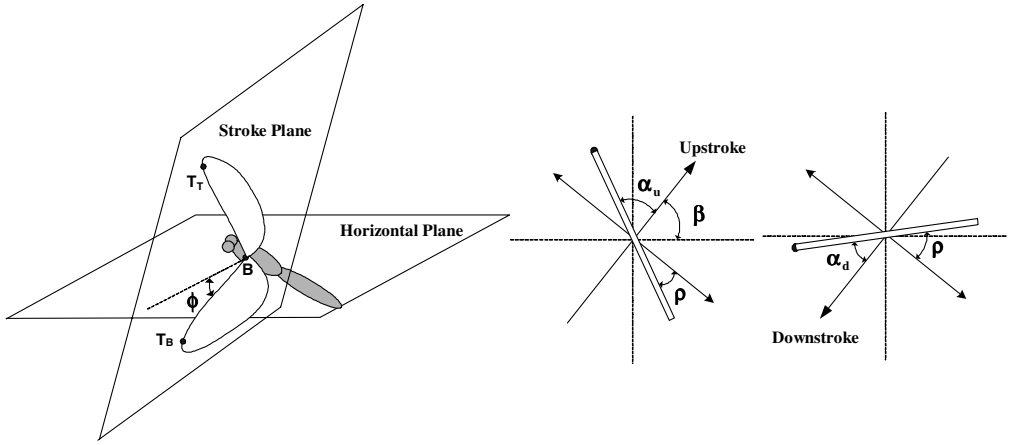

Fig. 6 Kinematic parameters.

The increasing circulation in the LEV from base to tip generates a pressure gradient in the core of the vortex, which is responsible for the observed spanwise flow [12].

A. Base Flows

Different rotation timings and their effect on vortex formation, and hence on lift and thrust, are summarized by Gopalakrishnan and Tafti [12] for $J = 0.5$. In the paper, advanced, symmetric, and delayed rotation kinematics are investigated with pure translation during the down and upstrokes, together with continuous rotation during the full cycle. For the purposes of this paper, advanced and continuous rotation are considered for their superior lift and thrust production and also for generating strong vortices during the flapping cycle.

1. Continuous Rotation with Advance Ratio, $J = 0.5$

Figures 10a and 10b show the variation of lift and thrust coefficient. The lift and thrust profiles during the downstroke are dominated by LEV dynamics. At $t^* = 0.1$, a spiral LEV starts forming near the tip and it is attached to the top surface of the wing. Further along the downstroke, the LEV extends across the span with an increase in size from base to tip, with a strong spanwise velocity through its core. The formation and strengthening of the LEV is reflected in the increase in lift and thrust until $t^* = 0.27$. Around $t^* = 0.2$, the interaction of the LEV with the tip vortex destabilizes the LEV and separation begins near the wing tip, and by $t^* = 0.3$, the initial LEV has moved downstream close to the wing top surface, and secondary LEVs are just beginning to form, which also lift off during the downstroke. Vorticity isosurfaces (Fig. 11) show that the LEV near the base is attached for most of the downstroke, whereas the part of the LEV near the tip sheds and dissipates into the flow during the end of the downstroke ($t^* = 0.4$ to 0.5). Since there is no well-defined supination in continuous rotation, and hence no rapid increase in α_{eff} (Fig. 9a), there is no secondary peak in lift during the downstroke.

During the upstroke, since α_{eff} (as shown in Fig. 9a from $t^* = 0.5$ to 1.0 at wing midspan) has low negative values for most of the wing surface, the effective flow is incident on the top surface, resulting in the formation of a small positive vortex on the bottom surface close to the wing tip. Around $t^* = 0.85$, the positive vortex on the bottom surface increases in size and begins to separate near the wing tip, resulting in a peak in negative lift (Fig. 10a) and a second positive thrust peak (Fig. 10b).

2. Continuous Rotation with Advance Ratio, $J = 1.0$

For the higher advance ratio, with the rest of the kinematics staying the same, the higher flow velocity results in a lower α_{eff} during the downstroke, whereas the upstroke has low positive α_{eff} for the majority of wingspan with low negative values closer to the wing tip. During the downstroke, this has the effect of slowing down the growth of the LEV, helping it to stay attached longer and shifting the peak in lift (Fig. 10a) and thrust (Fig. 10b) further in the time cycle. An interesting observation is that in spite of the lower α_{eff}, the faster flowfield combined with continuous rotation enables higher lift for the higher-advance-ratio flow.

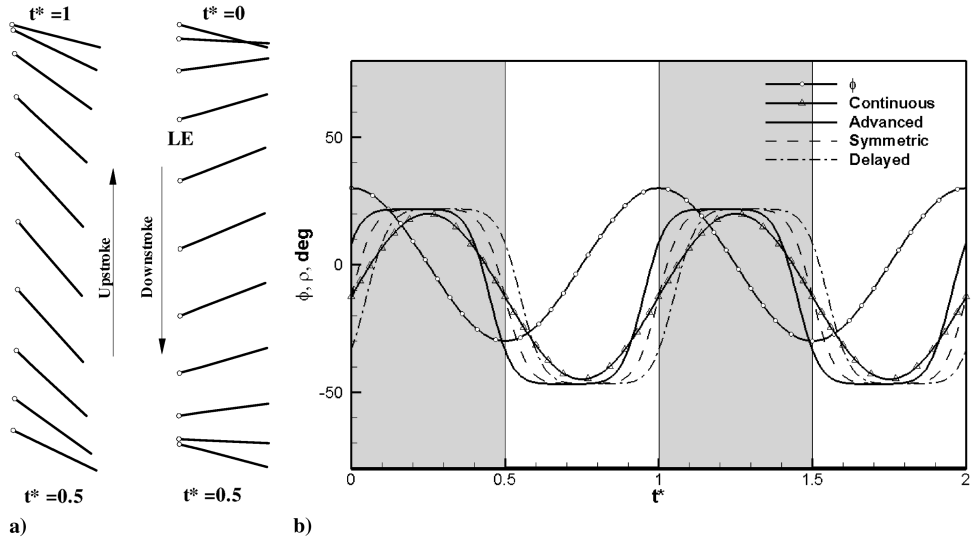

Fig. 7 Representation of wing kinematics in terms of a) wing midchord motion during one cycle with continuous rotation and b) flapping and rotation angles over a cycle. Shaded region represents downstroke.

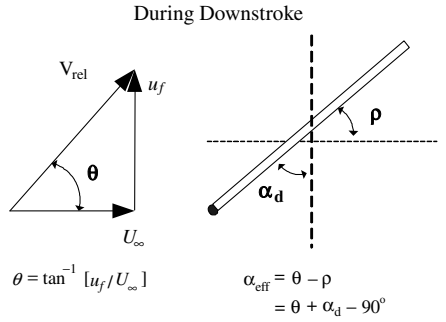

Fig. 8 Effective angle of attack during downstroke.

The change in α_{eff} from low negative to low positive during the upstroke (see Fig. 9a) is shown to be beneficial for lift generation, whereas it has a detrimental effect on thrust generation. During upstrokes, this is observed to be the consistent behavior of lift and thrust profiles when reacting to α_{eff} changes. In the absence of strong persistent LEVs, α_{eff} is shown to be the primary factor affecting lift and thrust. In essence, the continuous rotation and the lowered α_{eff} help develop stronger more sustained LEVs for higher-velocity flow during the downstroke, whereas for the upstroke, the LEVs are not a dominating factor in force production.

3. Advanced Rotation with Advance Ratio, $J = 0.5$

Figures 12a and 12b show the variation of lift and thrust coefficients for advanced rotation for $J = 0.5$ and $J = 1.0$. As shown in Fig. 8, for advanced rotation, the supination and pronation are short duration events at the end of the downstroke and upstroke, respectively. In addition to the change in α_{eff} in the first half of the downstroke (brought about by acceleration in u_f), the supination and pronation in advanced rotation also result in a rapid change in α_{eff} (see Fig. 9b). This in effect causes a secondary peak in lift and thrust to occur for an advanced rotation flow during supination and pronation, as shown in Figs. 12a and 12b. The lift profile for the base flow ($J = 0.5$) shows two peaks in lift during the downstroke, 1 in.

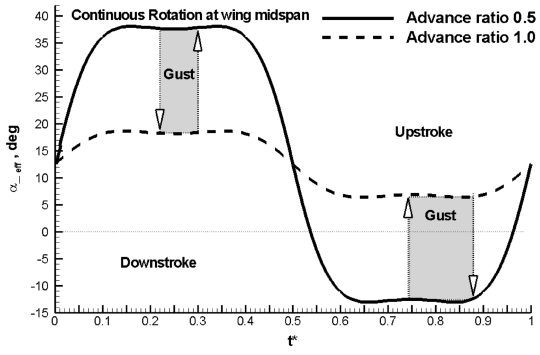

a)

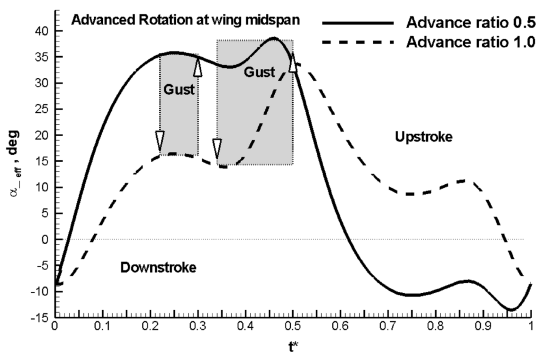

b)

Fig. 9 Effective angle of attack variation at midspan for a) continuous rotation and b) advanced rotation. Shaded region shows periods of gust application.

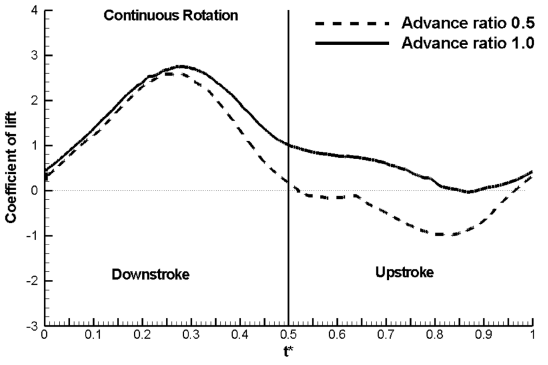

a)

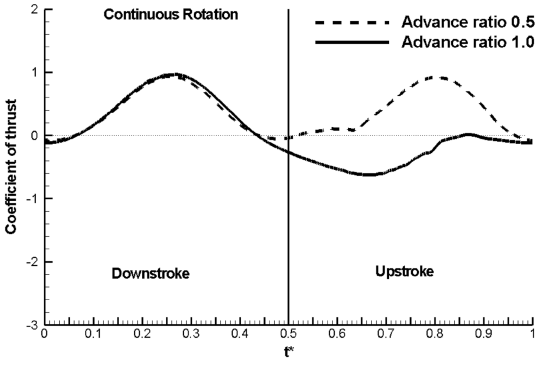

b)

Fig. 10 Profiles for continuous rotation under different advance ratios for a) lift and b) thrust.

the middle of the downstroke and another during supination. The rapid increase in α_{eff} during supination results in the formation of a vortex near the base, strengthening the LEV further. This results in a secondary peak in lift. However, due to the rotation, the contribution of the LEV to the thrust drops continuously and results in drag during the latter part of supination. The flow structures are similar to continuous flow except in the timing, development and strength of the LEVs formed.

4. Advanced Rotation with Advance Ratio, $J = 1.0$

As in continuous rotation, an increase in the approach velocity results in a lower α_{eff} during the downstroke with a corresponding increase from negative to positive values during the upstroke. Consequently, the variation of lift and thrust during the first half of the downstroke mimics that of $J = 0.5$, and is similar to the

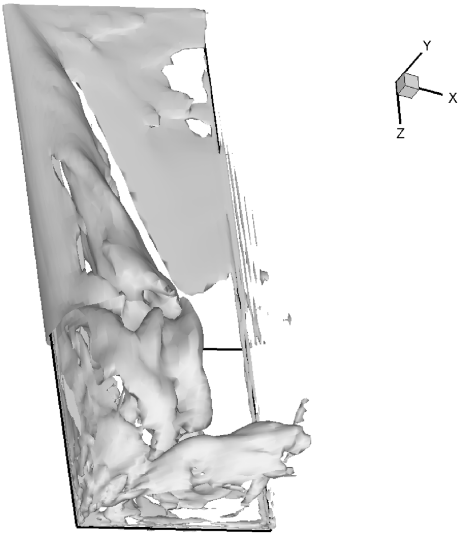

Fig. 11 Vorticity isosurface for continuous rotation at $t^* = 0.23$.

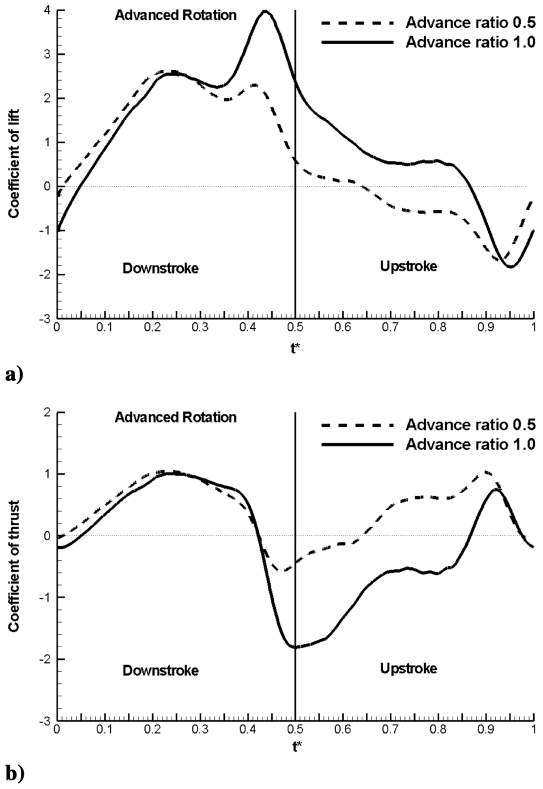

Fig. 12 Profiles of advanced rotation under different advance ratios for a) lift and b) thrust.

observations made earlier for continuous rotation. However, during supination and pronation, the relative change in α_{eff} is much larger at the higher advance ratio of $J = 1$ than it is for $J = 0.5$, as shown in Fig. 9b. It is noted that this higher rate of change of α_{eff} for $J = 1.0$ flow, even with lower absolute α_{eff} values, is shown to drive the secondary peak in lift well above the value of the lift in $J = 0.5$ flow (see Fig. 12a). This also has the effect of further strengthening the LEV or creating additional vortices on the top surface of the wing leading to a corresponding sharp decrease in thrust as the wing supinates. It is inferred that with wing rotation kinematics remaining constant across different advance ratio flows, the higher-velocity flow, $J = 1.0$, gives better dividends on force production during higher rate of change of α_{eff}. During the upstroke, the positive α_{eff} contributes to positive lift and negative thrust, until pronation changes α_{eff} and reverses the contribution to lift and thrust.

B. Effect of Gusts

The effect of short duration wind gusts of spatial extent much larger than the dimensions of the MAV are now studied by introducing a spatially uniform square waveform changing from $J = 0.5$ to 1.0. The gusts are applied from $t^* = 0.22$ until 0.30 during the fourth cycle for both continuous and advanced rotation during the downstroke. For advanced rotation another gust is applied from $t^* = 0.34$ until 0.5. For the upstroke, a gust is applied from $t^* = 0.74$ until 0.88 for continuous rotation. These particular intervals were chosen to map to corresponding peaks in lift in the regular flow to quantify the effect of the gust on the maximum instantaneous lift values and on the mechanisms responsible for the peaks in lift and thrust. To understand the effects of an inverted gust, freestream velocity changing from $J = 1.0$ to 0.5, we consider the intervals $t^* = 0.22$ to 0.3 in continuous rotation and $t^* = 0.34$ until 0.5 in advanced rotation. The timing and duration of the gusts for different flapping kinematics is summarized in Table 3.

As a prelude to the discussion that follows, in our observations, in addition to α_{eff}, the rate of change ($\mathrm{d}\alpha_{\text{eff}}/\mathrm{d}t$) is one of the other factors affecting instantaneous lift and thrust in the presence of LEVs for a hinged flapping wing. Formation, growth, and stability of the LEV, and hence lift and thrust in flapping flight, are influenced by $\mathrm{d}\alpha_{\text{eff}}/\mathrm{d}t$ during translation or rotation. In our observations, a rapid increase in α_{eff} leads to the strengthening of existing or the formation of new LEVs. Conversely, under the influence of a high-velocity gust, the sudden increase in advance ratio from 0.5 to 1.0 leads to a rapid decrease in α_{eff}. As Thomas et al. [28] have observed from tethered flow visualizations of dragonfly flight, rapid decreases in α_{eff} can induce vortex shedding at any stage from the flapping wing, affecting lift and thrust.

Table 3 Parameters used for different cases

Case	Rotation timing	Gust timing
A	Continuous	0.22–0.3
B	Continuous	0.74–0.88
C	Advanced	0.22–0.3
D	Advanced	0.34–0.5
E	Continuous, inverted gust	0.22–0.3
F	Advanced, inverted gust	0.34–0.5

1. *Case A: Continuous Rotation, Gust Between $t^* = 0.22$–0.3*

Figures 13a and 13b show the lift and thrust profiles, respectively, on gust application and removal for part of the cycle. On application of the gust at $t^* = 0.22$, there is a sharp instantaneous drop in lift and thrust. As shown in Fig. 9a, this is a result of the instantaneous drop in α_{eff}, from approximately 38° to about 18° at wing midspan, altering the diversion of air around the wing surface. For the nongust case at $J = 0.5$, the attached LEV has begun to shed and has started traveling downstream close to the wing surface, as shown in Figs. 14a and 14b. On gust application, the structure of this LEV does not change considerably at $t^* = 0.23$. However, the sudden velocity increase on both sides of the wing, due to the gust diminishes the circulation that contributes to lift and thrust production on the wing surface. With the application of the gust, the leading edge of the wing until 22% span has $\alpha_{\text{eff}} < 0$ and the low-pressure regions are significantly smaller on the top surface than without the gust. Thus, the sudden change in α_{eff} induces the existing LEV to detach and shed, further reducing the circulation around the wing.

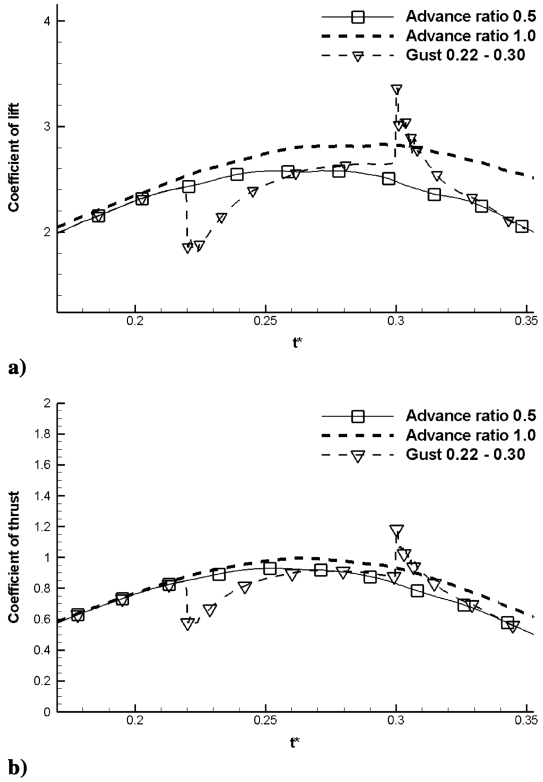

Fig. 13 Values in the case of continuous rotation with and without gust for a) lift coefficient C_L and b) thrust coefficient C_T.

After this initial drop, the lift quickly recovers and exceeds the lift of the base case at $t^* = 0.25$. Closer examination of the flow structure shows the formation of a fresh LEV at the leading edge, as the original LEV sheds but remains close to the wing surface as it convects downstream. Figures 15 and 16 contrast the pressure distribution and vorticity contours between the base flow and the gust flow at $t^* = 0.29$, respectively. In the base flow, we see a vortex core just separating close to the surface with a secondary vortex just beginning to manifest itself. In the gust-driven case, after the initial drop in circulation and the accelerated separation of the LEV, the higher-velocity flow accelerates the development of the flow. As a result, the secondary LEV is already well formed at $t^* = 0.29$, whereas the separated LEV approaches the trailing edge (Fig. 17). The gust can be considered akin to rapidly increasing the advance ratio of the flowfield. As shown in the higher-advance-ratio flow (see Sec. IV.A.2), the lowered α_{eff} and faster flow development lends itself to stronger

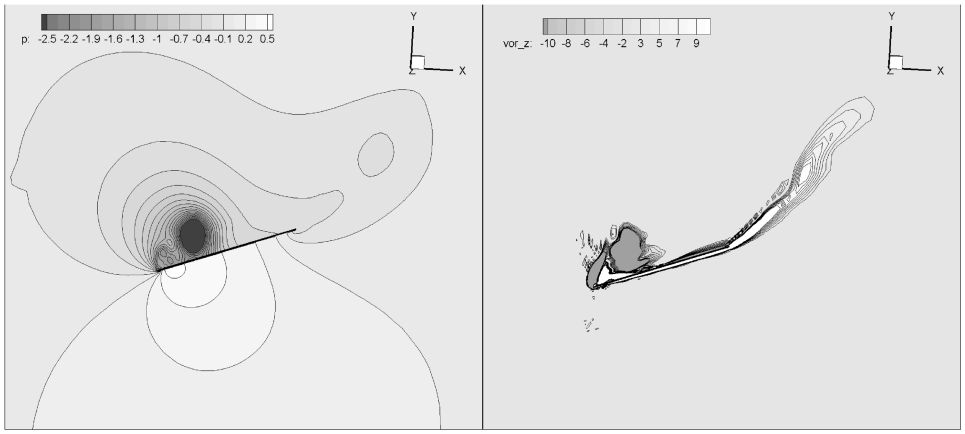

a) **b)**

Fig. 14 Continuous rotation without gust at $t^* = 0.23$ at location $\zeta = 2.1$ showing a) pressure contours and b) vorticity contours in z.

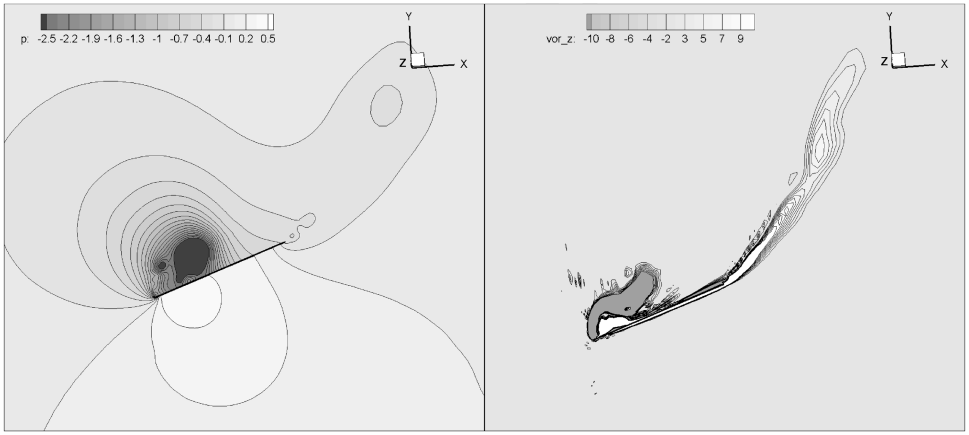

a) **b)**

Fig. 15 Continuous rotation without gust at $t^* = 0.29$ at location $\zeta = 2.1$ showing a) pressure contours and b) vorticity contours in z.

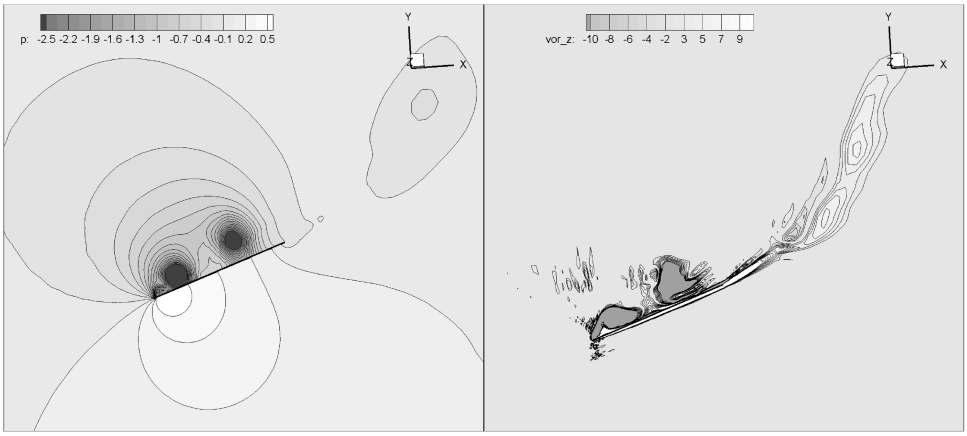

a) **b)**

Fig. 16 Continuous rotation with gust at $t^* = 0.29$ at location $\zeta = 2.1$ showing a) pressure contours and b) vorticity contours in z.

attached LEVs when wing rotation is in effect, increasing the transient circulatory forces around the wing. The two vortices on the surface of the wing eventually cause the lift and thrust profile of the gust-driven flow to exceed that of the base flow. This development emphasizes the impact of the LEV (delayed stall) on the instantaneous lift and thrust characteristics of the flapping wing during the downstroke.

After the gust is removed at $t^* = 0.3$, the lift and thrust values undergo a rapid increase, surpassing not only the base flow at $J = 0.5$ but also the values at $J = 1.0$. On gust mitigation, the α_{eff} increases rapidly, from $\cong 18^\circ$ to 38° at wing midspan and tends to fortify existing LEVs on the surface, thereby increasing and prolonging positive lift. The primary factor here, though, is the suddenly higher α_{eff} across the wing, which ensures that more of the wingspan contributes toward positive force production. This effect combined with residual vortices lends itself to a surfeit of low-pressure regions on the wing top surface. The rapid increase in α_{eff} across the wing leads to a greater volume of air being deflected by the wing, which in turn results in a increased pressure difference between the top and bottom surfaces of the wing, thereby increasing lift and thrust values. The residual separated vortex from gust-driven flow, which is almost at the trailing edge, is observed to suddenly get stronger at $t^* = 0.31$ when the gust is removed and lingers on the surface with the slower flow. In the base flow ($J = 0.5$), the LEV separates past wing midspan, whereas in the presence of the gust, it extends until the wing tip staying close to the surface (Fig. 18). But since it is a residual field, and no phenomenon is driving further development, the flow soon settles back to the base flow on removal of the gust.

2. *Case B: Continuous Rotation, Gust Between $t^* = 0.74$–0.88*

In this case, the gust is applied during the upstroke spanning the time interval when there is a peak in thrust and a trough in lift. The responses of lift and thrust to the gust are shown in Figs. 19a and 19b, respectively. As observed in Fig. 9a, the application of the gust changes α_{eff} from a negative to a positive value in which 62% of the wing now has a positive α_{eff}. Although the negative α_{eff} and the bottom surface LEV in the base flow was detrimental to lift production, the positive α_{eff} contributes to LEV formation on the wing top surface, which is conducive to lift but detrimental to thrust. Again, we find that α_{eff} has a strong impact on the lift and thrust characteristics of the wing without any phase lag between time of application of gust and its resultant effect on the wing characteristics.

During the upstroke in the base flow, the contribution of LEV to force production is much less prominent. Hence, with the application of the gust, the lift and thrust characteristics of the wing respond almost instantaneously to the change in α_{eff}, unlike the downstroke, where strong LEVs are present. Similarly, when the gust is removed at $t^* = 0.88$, the lift and thrust return to their normal profiles almost instantaneously, without showing any phase lag in force production, due to the absence of any prominent flow structures.

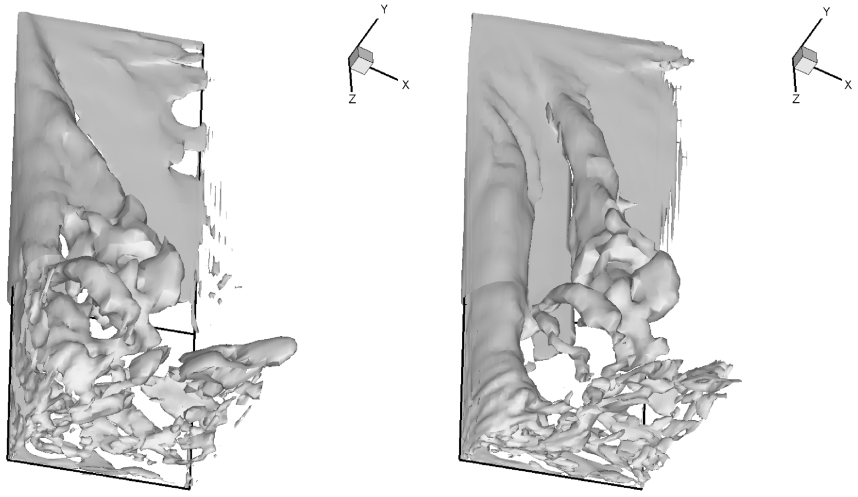

a) b)

Fig. 17 Continuous rotation at $t^* = 0.29$ showing isosurface of vorticity in z a) without gust and b) with gust.

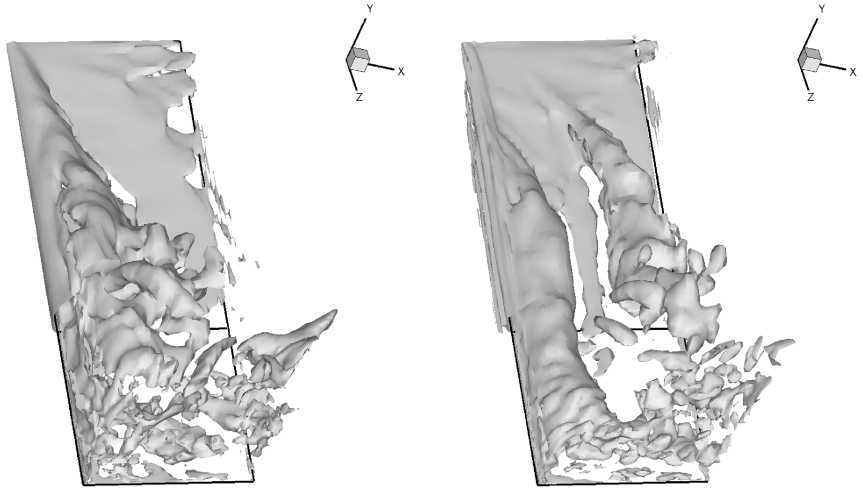

a) b)

Fig. 18 Continuous rotation at $t^* = 0.31$. Showing isosurface of vorticity in z a) without gust and b) with gust.

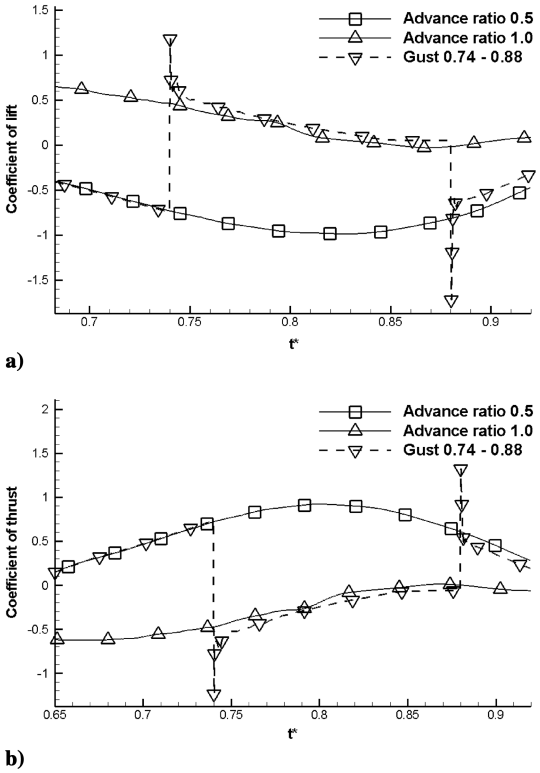

Fig. 19 Values in the case of continuous rotation with and without gust for a) lift coefficient C_L and b) thrust coefficient C_T.

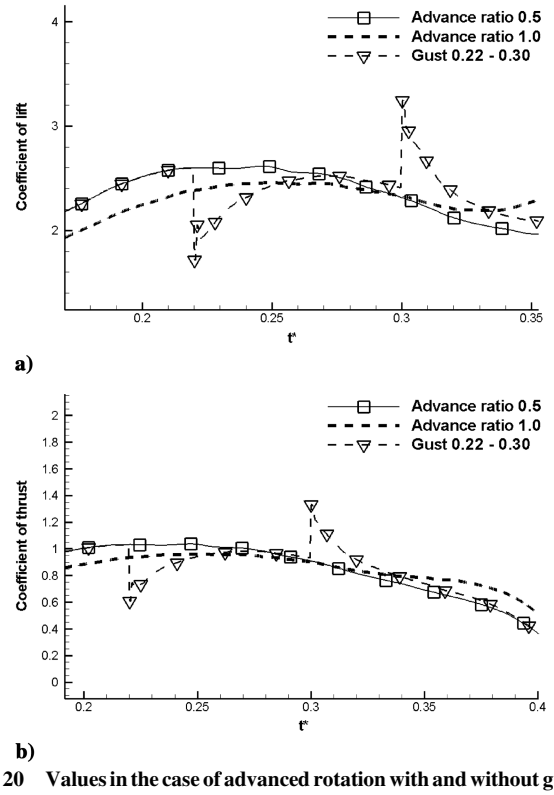

Fig. 20 Values in the case of advanced rotation with and without gust in case C for a) lift coefficient C_L and b) thrust coefficient C_T.

3. Case C: Advance Rotation, Gust Between $t^* = 0.22$–0.3

This case is similar to case A, with the only difference being the rotational kinematics. On application of the gust, α_{eff} drops from 34 to 16° at the wing midspan, which results in a sharp drop in lift and thrust. Just like in case A, the gust initiates the detachment of the existing LEV on the top surface of the wing with the formation of a secondary LEV. The ensuing dynamics of the LEVS in the presence of the gust and on gust removal are very similar to case A and hence are not repeated again. The behavior of the lift and thrust profiles is shown in Figs. 20a and 20b.

4. Case D: Advanced Rotation, Gust Between $t^* = 0.34$–0.5

From Fig. 7 it can be observed that for advanced rotation, $t^* = 0.33$ is around where supination starts and the gust is applied, spanning the supination until the end of the downstroke (see Fig. 9b). On application of the gust at $t^* = 0.34$, only slight losses in lift and thrust are observed, as shown in Figs. 21a and 21b, whereas α_{eff} drops sharply across the wing, from around 34 to 14° at wing midspan (see Fig. 9b). This behavior is markedly different from what has been observed thus far, wherein the losses in thrust and lift have been more significant. It stands to reason that supination, which is rapidly increasing the α_{eff}, is able to mitigate the effect of the gust application. The LEV structure at $t^* = 0.35$ for the non-gust-driven and gust-driven flows remains largely unchanged, with the LEV beginning to shed in the gust-driven flow.

After the initial drop, the lift is shown to recover quickly and follow the lift profile of the $J = 1.0$ base case. In effect, the gust rapidly transitions the flow from $J = 0.5$ to $J = 1.0$ base flow as far as the lift and thrust profiles are concerned (Figs. 21a and 21b). However, the actual flow structures in the gust-driven case are different from the $J = 1.0$ base flow. The wing rotation combined with the lowered α_{eff} and faster flow is shown to develop a stronger attached secondary LEV as the original LEV is convected downstream for the gust-driven case.

Originally, the secondary peak in lift occurred at $t^* = 0.42T$ for the advance ratio of 0.5 flow. The new peak for gust-driven flow is at $t^* = 0.44$. Figures 22 and 23 contrast the pressure distribution and vorticity contours between the base flow and the gust flow at $t^* = 0.44$, respectively. In the base flow ($J = 0.5$), the LEV is shown stretching from root until around midspan at $t^* = 0.44$ (Fig. 24a). After midspan, it is lifted off the surface and interacting with the wing-tip vortex. In the gust-driven case, we have two LEVs (Fig. 24b), both very close to the surface at $t^* = 0.44$. The first is the developed secondary LEV and the other is the separated vortex core approaching the trailing edge. The $J = 1.0$ base flow at $t^* = 0.44$ has

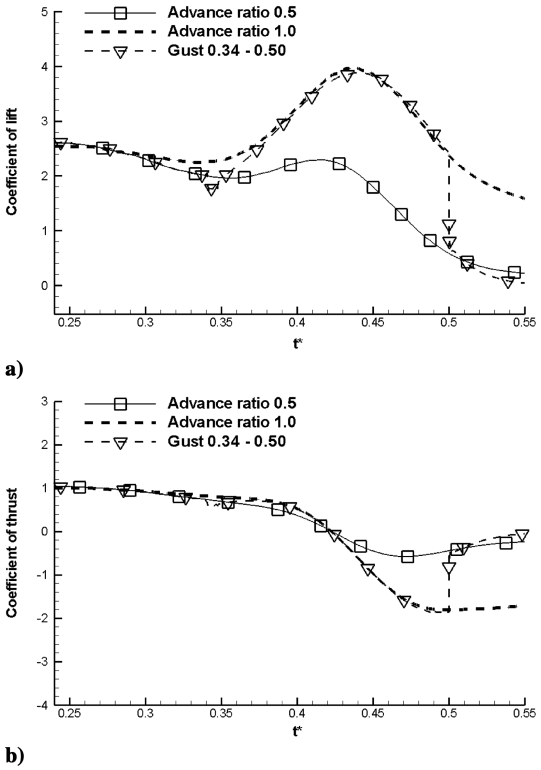

Fig. 21 Values in the case of advanced rotation with and without gust in case D for a) lift coefficient C_L and b) thrust coefficient C_T.

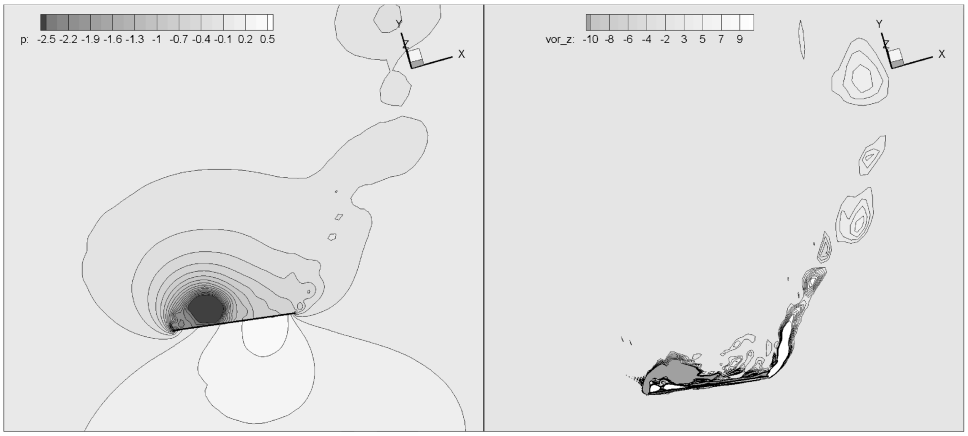

a) **b)**

Fig. 22 Advanced rotation without gust at $t^* = 0.44$ at location $\zeta = 2.1$ showing a) pressure contours and b) vorticity contours in z.

a) **b)**

Fig. 23 Advanced rotation with gust at $t^* = 0.44$ at location $\zeta = 2.1$ showing a) pressure contours and b) vorticity contours in z.

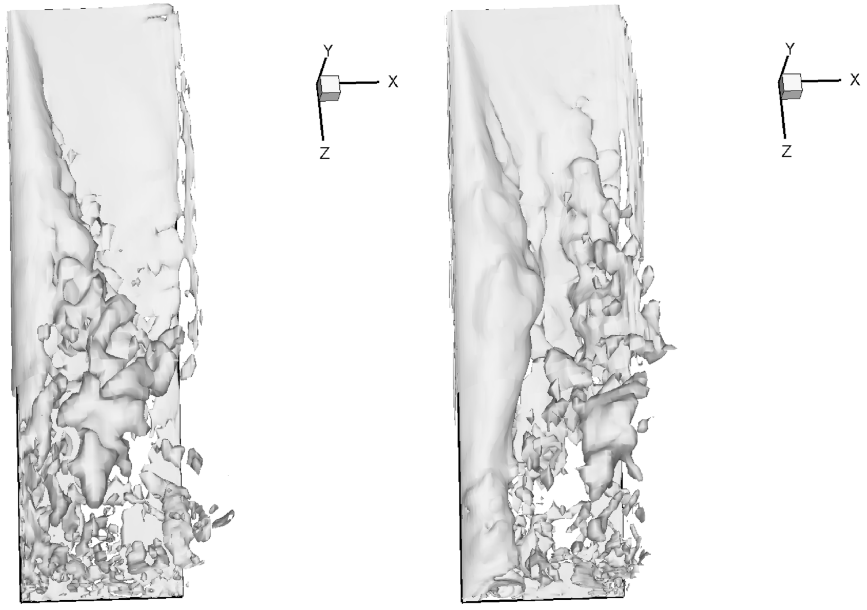

a) **b)**

Fig. 24 Advanced rotation at $t^* = 0.44$ showing isosurface of vorticity in z a) without gust b) with gust.

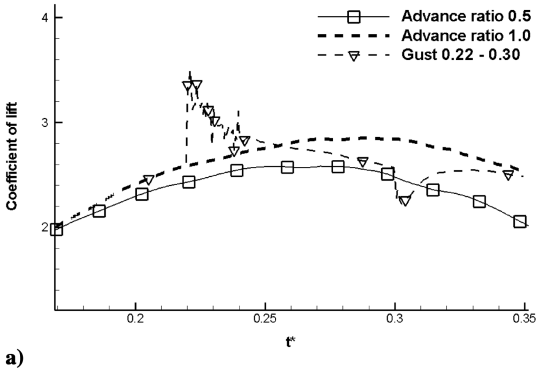

a)

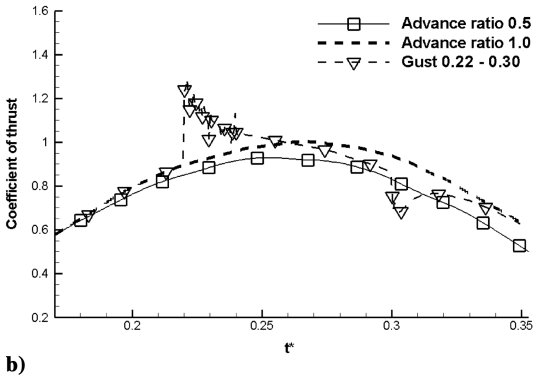

b)

Fig. 25 Values in the case of continuous rotation with and without inverted gust for a) lift coefficient C_L and b) thrust coefficient C_T.

a single LEV on the surface, yet the gust-driven case and the base case have similar lift and thrust profiles. We infer that the force production mechanism during supination is less dependent on the transient LEV dynamics (delayed stall) and is possibly better explained by the rotational circulation theory.

As soon as the gust is removed at $t^* = 0.5$, coinciding with the start of the upstroke, we see the lift and thrust profiles drop back to the advance ratio of 0.5 flow curve quite abruptly. At this point, the downstroke LEVs have been shed and the wing is at rest, whereas wing rotation (supination) is still going on and the slower flow mainly reacts to the change in α_{eff} during the upstroke, as we have seen before. This behavior is quite different from the characteristics of the flow seen in the removal of gust during the downstroke. In those cases, we found that after the immediate jump brought about by the rapid α_{eff} change, the transient creation/separation of LEVs (delayed stall) further sustained the change in lift and thrust profiles. Here, in the absence of LEVs during the initial part of the upstroke, we see only a reaction to the effective AOA change.

5. Case E: Continuous Rotation, Inverted Gust Between $t^* = 0.22$–0.3

The application of gust, in this case simulated as an inverted square wave that decreases freestream velocity, drops the advance ratio from 1.0 to 0.5. There is a sharp instantaneous increase in lift and thrust profile at $t^* = 0.22$, as shown in Figs. 25a and 25b. Similar to case A, this can be attributed to the sudden increase in α_{eff} across the wing, from approximately 18° to about 38° at wing midspan (Fig. 9a). Higher α_{eff} across the wing ensures that more of the wingspan contributes toward positive force production. A significant difference in this gust scenario is that since α_{eff} is increasing, there is no immediate LEV shedding into the flow. As a result of this, combined with the slower velocity in the freestream, the circulation in the vicinity of the wing is sustained through the gust. Hence, lift and thrust profiles greater than the base flow ($J = 1.0$) are observed until around $t^* = 0.26$, when the profiles start falling back to the $J = 0.5$ flow values.

Examination of the flow structures past $t^* = 0.29$, shown in Fig. 26, reveal the existing LEV still on the wing top surface but separating close to the wing tip, due to the high α_{eff}. In the base flow ($J = 1.0$) a secondary LEV is beginning to form, whereas the original LEV is increasing in strength and stretches the full span of the wing, due to the prevalent low α_{eff}. The above changes again exemplify the influence of the delayed stall phenomena on lift and thrust profiles, due to changing and sustained LEV structures during the translational part of the downstroke.

On gust mitigation, the α_{eff} again drops back to the base flow values and we see a corresponding drop in force production. With the sudden decrease in α_{eff}, similar to cases A–D, the existing LEV is observed to begin shedding and is downstream away from the wing surface by $t^* = 0.33$, whereas a weaker secondary LEV is beginning to form. In the base flow ($J = 1.0$) the original vortex is still attached to the leading edge.

6. Case F: Advanced Rotation, Inverted Gust Between $t^* = 0.34$–0.5

This case was considered to check the effect of inverted gust on the $J = 1.0$ base flow during supination. Similar to case D, Figs. 27a and 27b show that the lift and thrust profiles are shown to be less affected by the application of the gust, and the flow recovers very quickly and transitions to the $J = 0.5$ from the base flow of $J = 1.0$. This reinforces our inference that the rotational circulation phenomena better explains the force production mechanism during supination rather than transient LEV dynamics.

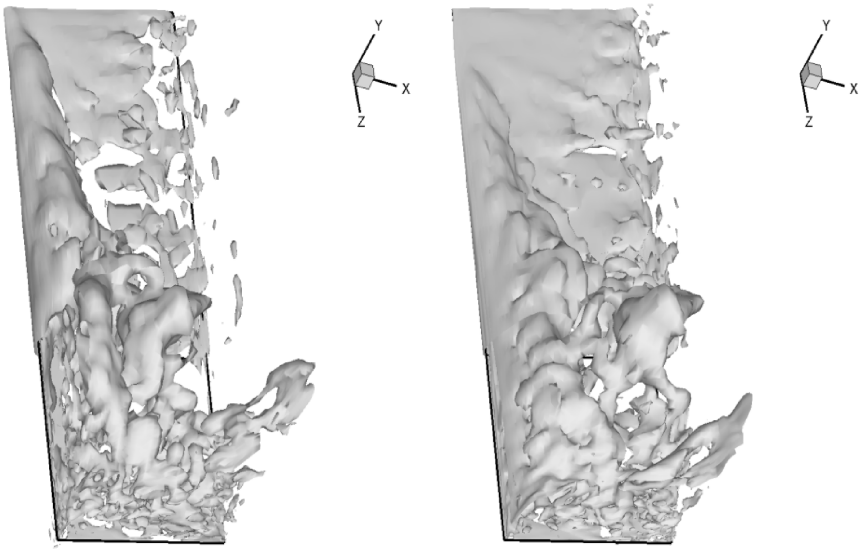

a) b)

Fig. 26 Continuous rotation at $t^* = 0.29$ for $J = 1.0$ flow showing isosurface of vorticity in z a) without gust and b) with inverted gust.

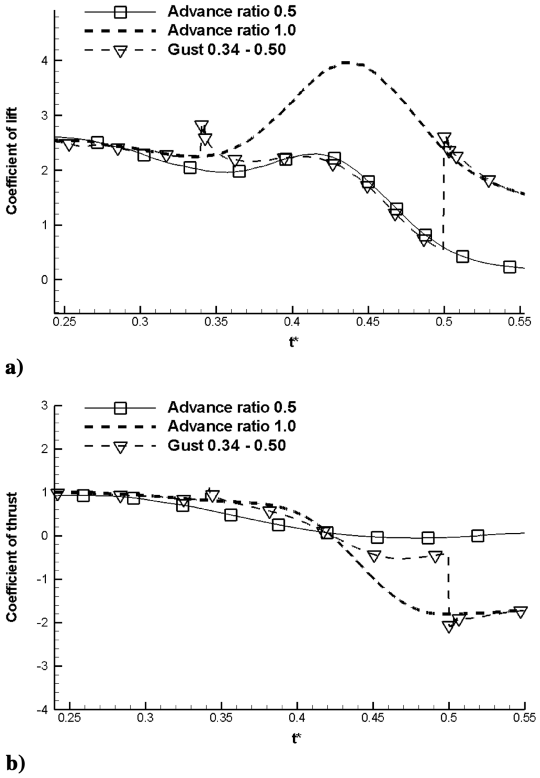

Fig. 27 Values in the case of advanced rotation with and without inverted gust for a) lift coefficient C_L and b) thrust coefficient C_T.

At $t^* = 0.34$ when the gust is initiated, the α_{eff} suddenly increases across the wing, from around 14 to 34° at wing midspan. No immediate shedding of LEV is observed, which is consistent with case E. Similarly, since the flow is slower, the circulation in the vicinity of the wing is not immediately changed by the gust and this provides better force production initially. By $t^* = 0.4$ the gust-driven flow has transitioned fully to the $J = 0.5$ flow with similar lift and thrust profiles. At this point, the LEV dynamics are not shown to affect the force production. At $t^* = 0.5$, the upstroke characteristics takeover similar to case D and we see the force primarily reacting to α_{eff} change.

V. Conclusions

The present study contributes to the understanding of the effect of gusts on transient flow structures that characterize force production in flapping flight. The effect of timing and duration of gusts with different wing kinematics and rotation timings are investigated. Two different gusts, simulated as step functions in freestream velocity, are considered: one doubling the freestream velocity and the other halving it.

A key finding in this study is that the instantaneous lift and thrust profiles are influenced by the effective angle of attack α_{eff}, which is a function of the local flapping velocity, the approach freestream velocity, and the geometric angle of attack, and the LEV structures existing in the flow at any given time, with the LEVs themselves being influenced by the magnitude and rate of change in α_{eff}.

The behavior of lift and thrust are found to follow similar changes in all cases for gusts applied during the downstroke. For the gust cases in which freestream velocity is doubled, a loss in lift and thrust is initially realized, due to the rapid decrease in α_{eff} and the disruption of the circulation around the wing by the suddenly faster freestream, together with separation of the LEV. Frontal gusts applied during the downstroke are then shown to accelerate the development of the flow, resulting in the formation and detachment of multiple LEVs on the wing surface that increase the lift and thrust. As the gust-driven flow progresses, depending on the wing kinematics and rotation, we observe the lift profile of the gust-driven flow to exceed or lie between the two base flows. Cases with multiple gust-induced LEVs on the wing surface illustrate the importance of LEV dynamics in force production by eventually exceeding the base flow performance as the flow develops. Contrary to the gust response during the downstroke, the upstroke lift and thrust profiles react primarily to the changing α_{eff} on gust application with opposite variations.

Conversely, application of an inverse gust is characterized by an initial increase in lift and thrust production, due to the sudden increase in α_{eff}, with the circulation around the wing sustained through the gust without LEV separation. But as the slower gust-driven flow develops, the initial strong circulation dies out in the slower freestream and force production falls below the base flow performance ($J = 1.0$), tending toward the $J = 0.5$ curve.

It is noted that the effect of gusts on lift and thrust during the downstroke is diminished when applied during rapid supination. Further, the transient LEV dynamics are shown not to play a major part in the force production during supination, as evidenced by the lack of change shown in lift and thrust production, even with changes in the flow structure. We conclude that rotational circulation, which is a major contributor for force generation just before stroke changes, dominates here.

As is evident from the above results, wing kinematics and the timing and duration of gusts will determine the extent of the changes in the flow structure. For a given wing configuration (wing shape, stroke plane, rotation axis, and flapping amplitude) it might be possible to arrive at approximate upper and lower bounds for lift and thrust production in response to gusts by using the force profiles of the corresponding advance ratio flows and allowing for an empirically determined deviation from those. Based on the variations shown within the scope of this paper, such an approximation should hold well across different wing kinematics and gusts.

Acknowledgment

The financial support of the U.S. Army Research Office under award number C: W911NF-08-1-0433 is gratefully acknowledged.

References

[1] Watkins, S., Milbank, J., and Loxton, B. J., "Atmospheric Winds and Their Implications for Microair Vehicles," *AIAA Journal*, Vol. 44, No. 11, 2006, pp. 2591–2600. doi:10.2514/1.22670

[2] Weis-Fogh, T., "Quick Estimate of Flight Fitness in Hovering Animals, Including Novel Mechanisms for Lift Production," *Journal of Experimental Biology*, Vol. 59, 1973, pp. 169–230.

[3] Dickinson, M. H., and Götz, K. G., "Unsteady Aerodynamic Performance of Model Wings at Low Reynolds Numbers," *Journal of Experimental Biology*, Vol. 174, 1993, pp. 45–64.

[4] Dickinson, M. H., Lehmann, F.-O., and Sane, S. P., "Flight Wing Rotation and the Aerodynamic Basis of Insect Flight," *Science*, Vol. 284, No. 5422, June 1999, pp. 1954–1960. doi:10.1126/science.284.5422.1954

[5] Walker, J. A., "Rotational Lift: Something Different or More of the Same?," *Journal of Experimental Biology*, Vol. 205, 2002, pp. 3783–3792.

[6] Sun, M., and Tang, J., "Unsteady Aerodynamic Force Generation by a Model Fruit Fly Wing in Flapping Motion," *Journal of Experimental Biology*, Vol. 360, 2002, pp. 55–70.

[7] Sun, M., and Yu, X., "Aerodynamic Force Generation in Hovering Flight in a Tiny Insect," *AIAA Journal*, Vol. 44, No. 7, 2006, pp. 1532–1540. doi:10.2514/1.17356

[8] Liu, H., Ellington, C. P., Kawachi, K., Berg, C. V. D., and Willmottl, A. P., "A Computational Fluid Dynamic Study of Hawkmoth Hovering," *Journal of Experimental Biology*, Vol. 201, 1998, pp. 461–477.

[9] Ramamurti, R., and Sandberg, W. C., "A Three-Dimensional Computational Study of the Aerodynamic Mechanisms of Insect Flight," *Journal of Experimental Biology*, Vol. 205, 2002, pp. 1507–1518.

[10] Ansari, S. A., Knowles, K., and Żbikowski, R., "Insectlike Flapping Wings in the Hover Part 2: Effect of Wing Geometry," *Journal of Aircraft*, Vol. 45, No. 6, 2008, pp. 1976–1990. doi:10.2514/1.35697

[11] Ansari, S. A., Knowles, K., and Żbikowski, R., "Insectlike Flapping

Wings in the Hover Part 1: Effect of Wing Kinematics," *Journal of Aircraft*, Vol. 45, No. 6, 2008, pp. 1945–1954. doi:10.2514/1.35311

[12] Gopalakrishnan, P., and Tafti, D. K., "Effect of Rotation Kinematics and Angle of Attack on Flapping Flight," *AIAA Journal*, Vol. 47, No. 11, 2009, pp. 2505–2519. doi:10.2514/1.37540

[13] Ellington, C. P., "The Novel Aerodynamics of Insect Flight: Applications to Micro-Air Vehicles," *Journal of Experimental Biology*, Vol. 202, 1999, pp. 3439–3448.

[14] Gopalakrishnan, P., and Tafti, D. K., "Effect of Reynolds Number, Tip Shape, and Stroke Deviation on Flapping Flight," 39th AIAA Fluid Dynamics Conference, San Antonio, TX, AIAA Paper 2009-4193, 2009.

[15] Birch, J. M., Dickson, W. B., and Dickinson, M. H., "Force Production and Flow Structure of the Leading Edge Vortex on Flapping Wings at High and Low Reynolds Numbers," *Journal of Experimental Biology*, Vol. 207, No. 7, 2004, pp. 1063–1072. doi:10.1242/jeb.00848

[16] Gopalakrishnan, P., and Tafti, D. K., "Effect of Wing Flexibility on Lift and Thrust Production in Flapping Flight," *AIAA Journal*, Vol. 48, No. 5, May 2010, pp. 865–877. doi:10.2514/1.39957

[17] Ramamurti, R., and Sandberg, W., "Computations of Insect and Fish Locomotion with Applications to Unconventional Unmanned Vehicles," *AIAA Journal*, Vol. 46, No. 9, 2008, pp. 2178–2190. doi:10.2514/1.32826

[18] Lian, Y., and Shyy, W., "Aerodynamics of Low Reynolds Number Plunging Airfoil Under Gusty Environment," 45th AIAA Aerospace Sciences Meeting and Exhibit, Reno, NV, AIAA Paper 2007-71, 2007.

[19] Gopalan, H., and Povitsky, A., "A Numerical Study of Gust Suppression by Flapping Airfoils," 26th AIAA Applied Aerodynamics Conference, Honolulu, HI, AIAA Paper 2008-6394, 2008.

[20] Germano, M., Piomelli, U., Moin, P., and Cabot, W. H., "A Dynamic Subgrid-Scale Eddy Viscosity Model," *Physics of Fluids*, Vol. 3, 1991, pp. 1760–1765. doi:10.1063/1.857955

[21] Demirdzic, I., and Peric, M., "Space Conservation Law in Finite Volume Calculation of Fluid Flow," *International Journal for Numerical Methods in Fluids*, Vol. 8, No. 9, 1988, pp. 1037–1050. doi:10.1002/fld.1650080906

[22] Demirdzic, I., and Peric, M., "Finite Volume Method for Prediction of Fluid Flow in Arbitrarily Shaped Domains with Moving Boundaries," *International Journal for Numerical Methods in Fluids*, Vol. 10, No. 7, 1990, pp. 771–790. doi:10.1002/fld.1650100705

[23] Gopalakrishnan, P., and Tafti, D. K., "A Parallel Multiblock Boundary-Fitted Dynamic Mesh Solver for Simulating Flows with Complex Boundary Movement," *Computers and Fluids*, Vol. 38, No. 8, 2009, pp. 1592–1607. doi:10.1016/j.compfluid.2009.01.006

[24] Lai, J. C. S., and Platzer, M. F., "Jet Characteristics of a Plunging Airfoil," *AIAA Journal*, Vol. 37, No. 12, 1999, pp. 1529–1537. doi:10.2514/2.641

[25] Heathcote, S., Wang, Z., and Gursul, I., "Effect of Spanwise Flexibility on Flapping Wing Propulsion," 36th AIAA Fluid Dynamics Conference and Exhibit, San Francisco, AIAA Paper 2006-2870, 2006.

[26] Gopalakrishnan, P., and Tafti, D. K., "Effect of Phasing of Rotation on Delayed Stall in Flapping Flight Related to Mavs at $Re = 10000$," AIAA 38th Fluid Dynamic Conference, Seattle, WA, AIAA Paper 2008-4301, 2008.

[27] Sane, S. P., and Dickinson, M. H., "The Control of Flight Force by a Flapping Wing: Lift and Drag Production," *Journal of Experimental Biology*, Vol. 204, 2001, pp. 2607–2626.

[28] Thomas, A. L. R., Taylor, G. K., Srygley, R. B., Nudds, R. L., and Bomphrey, R. J., "Dragonfly Flight: Free-Flight and Tethered Flow Visualizations Reveal a Diverse Array of Unsteady Lift-Generating Mechanisms, Controlled Primarily Via Angle of Attack," *Journal of Experimental Biology*, Vol. 207, No. 24, 2004, pp. 4299–4323. doi:10.1242/jeb.01262

M. Visbal
Associate Editor